

Quantifying Model Predictive Uncertainty with Perturbation Theory

Rishabh Singh

Jose C. Principe

Computational NeuroEngineering Lab (CNEL)
University of Florida
Gainesville, Florida, USA
rish283@ufl.edu, principe@cnel.ufl.edu

Abstract

We propose a framework for predictive uncertainty quantification of a neural network that replaces the conventional Bayesian notion of weight probability density function (PDF) with a physics based *potential field* representation of the model weights in a Gaussian reproducing kernel Hilbert space (RKHS) embedding. This allows us to use perturbation theory from quantum physics to formulate a moment decomposition problem over the model weight-output relationship. The extracted moments reveal successive degrees of regularization of the weight potential field around the local neighborhood of the model output. Such localized moments represent well the PDF tails and provide significantly greater accuracy of the model's predictive uncertainty than the central moments characterized by Bayesian and ensemble methods or their variants. We show that this consequently leads to a better ability to detect false model predictions of test data that has undergone a *covariate shift* away from the training PDF learned by the model. We evaluate our approach against baseline uncertainty quantification methods on several benchmark datasets that are corrupted using common distortion techniques. Our approach provides fast model predictive uncertainty estimates with much greater precision and calibration.

Deep neural network (DNN) models have become the predominant choice for pattern representation in a wide variety of machine learning applications due to their remarkable performance advantages in the presence of large amount data (LeCun et al., 2015). The increased adoption of DNNs in safety critical and high stake problems such as medical diagnosis, chemical plant control, defense sys-

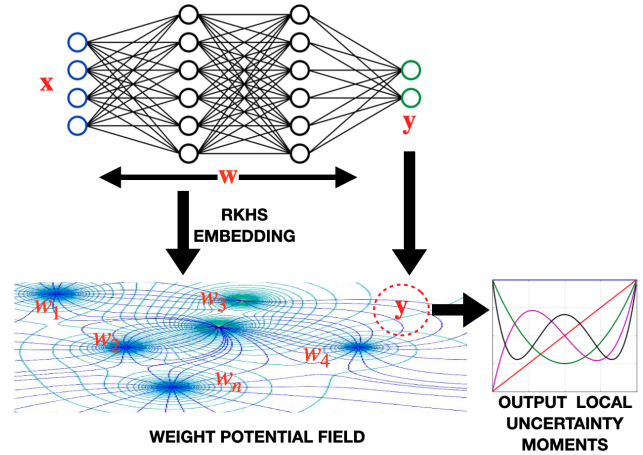


Figure 1: Proposed approach: Moments extracted from the local interaction of the model output with the RKHS potential field of the weights quantify the output uncertainty.

tems and autonomous driving has led to growing concerns within the research community on the *performance trustworthiness* of such models (Kendall & Gal, 2017; Lundberg & Lee, 2017). This becomes particularly imperative in situations involving data distributional shifts or the presence of out of distribution data (OOD) during testing towards which the model may lack robustness due to poor choice of training parameters or lack of sufficiently labeled training data, especially since machine learning algorithms do not have extensive prior information like humans to deal with such situations (Amodei et al., 2016). An important way through which trust in the performance of machine learning algorithms (particularly DNNs) can be established is through accurate techniques of *predictive uncertainty quantification* of models that allow practitioners to determine how much they should rely on model predictions.

Although there have been several categories of methods developed in the recent years, the Bayesian approach

(MacKay, 1992; Neal, 2012; Bishop, 1995) had for long been regarded as the gold standard for natural representation of uncertainty in neural networks. However, it has been realized that they are unable to scale to modern applications and often fail to capture the true data distribution in practice (Lakshminarayanan et al., 2017). Another fundamental limitation of Bayesian techniques is that they are only capable of selecting measurements of *central tendency* from the posterior. This limits their sensitivity in quantifying local uncertainty information which is especially prevalent in modern applications where models can capture very complex patterns with significant local variations.

We propose an approach for model uncertainty quantification that relies on the density and local fit criteria (Leonard et al., 1992) which in this context means that a model prediction y is reliable/certain only if the model has been trained to make predictions in the local vicinity of y (i.e. the model is *locally* regularized around y). To quantify the model space according to this criteria, one requires a rich localized representation of the model predictive PDF $p(y|\mathbf{w})$ which deems a prediction y reliable only if $\delta = p(y + \Delta y|\mathbf{w}) - p(y|\mathbf{w}) \approx 0$ where Δy is a small perturbation around y . Towards this end, we utilize an uncertainty decomposition framework called the quantum information potential field (QIPF) (Singh & Principe (2020); Singh & Principe (2021)) through which we represent the model weight space as a potential field by embedding the weights in a Gaussian reproducing kernel Hilbert space (RKHS). Such a representation (depicted in Fig. 1) allows us to principally use the notion of perturbation theory in quantum physics to quantify the local gradients of the model’s predictive PDF space in terms of multiple uncertainty moments, thereby giving a high resolution description of δ . In essence, these moments successively quantify the degree of regularization of the weights in the local neighborhood of the model output. The QIPF framework, which was first introduced by (Singh & Principe (2020); Singh & Principe (2021)), has shown promising (albeit very preliminary) results in model uncertainty quantification for regression problems (Singh & Principe, 2021) and in particular applications of time series analysis (Singh & Principe, 2020). It enjoys the following advantages over other methods:

- The QIPF utilizes the Gaussian RKHS whose mathematical properties, specifically the kernel trick (Smola & Schölkopf, 1998) and the kernel mean embedding theory (Muandet et al., 2017), makes it a universal injective estimator of data PDF and without making any underlying assumptions.
- Through its physics based moment decomposition formulation, it is able to provide a multi-scale description of the local PDF dynamics that focuses on the tail regions of the PDF thereby providing a very accurate description of uncertainty.

- It is also significantly simpler to compute and more scalable than Bayesian approaches. It is non-intrusive to the training process of the model and enables a *single-shot* estimation of model uncertainty at each test instance thereby offering practical advantages over ensemble and Monte Carlo approaches.

Our main contributions in this paper are three-fold:

- We use perturbation theory to provide a more concrete description of the QIPF framework and provide a new insight into how a potential field viewpoint of the model weight space can be used to describe the degree of regularization/certainty of trained weights in the local neighborhood of the output in terms of multiple moments.
- We specifically evaluate the performance of the framework in an important and unsolved problem of model uncertainty quantification in situations involving *co-variate shift* in test data.
- We analyze the performance of the QIPF against baselines of multiple UQ approaches using diverse models trained on benchmark datasets. We use both accuracy as well as calibration metrics to evaluate performance.

1 RELATED WORK

Existing methods for model uncertainty quantification can be broadly classified into Bayesian (MacKay, 1992; Neal, 2012; Bishop, 1995) and non-Bayesian techniques (Tibshirani, 1996; Osband et al., 2016; Pearce et al., 2018). Early Bayesian methods involving inference over model weights include Markov-chain Monte Carlo based Bayesian neural networks (Bishop, 1995), Hamiltonian Monte Carlo (Neal, 2012) and Laplacian approximation (MacKay, 1992). Although mathematically grounded, their applicability towards large datasets and model architectures becomes restrictive due to huge computational overheads involved. Faster variational inference based methods were developed later on to increase the training speed and efficiency of Bayesian neural networks (Graves, 2011; Paisley et al., 2012; Hoffman et al., 2013). However, such methods still suffer from high dimensionality and high complexity of weight associations making them infeasible for efficient learning of parameter dependencies (Pradier et al., 2018). Deterministic ReLU networks (which are very popular today) on the other hand suffer from arbitrarily high confidence in predictions outside training PDF (Hein et al., 2019; Guo et al., 2017). Therefore, some recent approaches attempt to approximate the posterior of deterministic networks in a *partially* Bayesian manner such as stochastic weight averaging (Izmailov et al., 2018), constructing a Gaussian distribution over

the weights (Kristiadi et al., 2020) and by fitting a Gaussian distribution over stochastic gradient descent iterations (Maddox et al., 2019). Khan et al. (2018) attempts to approximate Bayesian uncertainty of models by leveraging perturbation of weights during SGD. Other partial Bayesian approaches include (Malinin & Gales, 2018; Gast & Roth, 2018). Another category of uncertainty estimation methods include post-hoc calibration of networks to improve uncertainty estimation (Guo et al., 2017; Kuleshov et al., 2018). However, their performance range outside of training PDF is limited. Non-Bayesian techniques include ensemble based methods that aggregate outputs of multiple differently initialized models to give probabilistic outputs. A significant work in this line is that of Lakshminarayanan et al. (2017), where authors use deep ensemble neural networks to quantify output uncertainty. This method often produces the best results in many applications. Lu et al. (2020) attempts to simulate ensemble models by integrating over a constructed Gaussian distribution of models. Another work attempts to quantify uncertainty using an ensemble of optimal loss surface paths of a neural network (Garipov et al., 2018). A popular work by Gal & Ghahramani (2016) suggest to use Monte Carlo Dropout during model testing as an efficient way of extracting output uncertainty information.

2 PROBLEM FORMULATION AND BACKGROUND

We define the problem setup as follows. Let us assume that $x_i \in \mathbb{R}^d$ represents d dimensional input features and $y_i \in \{1 \dots k\}$ represents the target labels for k -class classification. We represent the training dataset with \mathbf{D} which consists of N i.i.d samples so that $\mathbf{D} = \{x_i, y_i\}_{i=1}^N$. We further denote the unknown probability density function observed through samples of \mathbf{D} (i.e. the true distribution of the classification problem) as $p^*(x, y)$. We assume a neural network parameterized by \mathbf{w} and trained on \mathbf{D} to model the conditional distribution $p(y|x, \mathbf{w})$, where \mathbf{w} is learnt from the training set. Let us further assume the training input samples to be governed by an unknown distribution $p(x|\lambda)$. Our goal is to quantify the predictive uncertainty of the trained neural network model on a test set whose governing PDF has undergone a shift from $p(x|\lambda)$ to become another unknown distribution $p(x|\gamma)$, while the target conditional distribution, $p(y|x)$, remains the same. This is also known as *covariate shift* (Quinero-Candela et al., 2009).

Epistemic uncertainty in neural networks, especially in regions of data outside of the training data PDF, arises from the degree of its bias-variance trade-off and hence depends how well a network's weights have been regularized for a given set of training samples. For a network that learns without any regularization, the optimization

problem corresponds to a maximum log-likelihood estimation problem given by $p(\mathbf{D}|\mathbf{w}) = \prod_i p(y^i|x^i, \mathbf{w})$. For regularized training of a network, the optimization corresponds to a maximum a-posteriori estimation problem of the weights given by $p(\mathbf{w}|\mathbf{D}) \propto p(\mathbf{D}|\mathbf{w})p(\mathbf{w})$, where the prior over weights $p(\mathbf{w})$ introduces regularization. Both cases still involve point prediction neural networks. The most optimal way of regularizing a network is by making no assumptions on the distribution of weights $p(\mathbf{w})$ which corresponds to an inference problem given by $p(\mathbf{w}|\mathbf{D}) = \frac{p(\mathbf{D}|\mathbf{w})p(\mathbf{w})}{\int p(\mathbf{D}|\mathbf{w})p(\mathbf{w})d\mathbf{w}}$ through a marginalization over \mathbf{w} . The posterior predictive distribution corresponding to an unknown data pair $\{x^*, y^*\}$ then becomes the following:

$$p(y^*|x^*, D) = \int p(y^*|x^*, \mathbf{w})p(\mathbf{w}|\mathbf{D})d\mathbf{w} \quad (1)$$

Although such a posterior is a theoretically elegant solution, it is intractable in most modern applications because of the difficulty in computing $p(\mathbf{w}|\mathbf{D})$. Variational inference and MCMC type approaches and their faster variants are typically implemented to obtain approximate solutions. Variational inference posits a variational family of distributions (using a latent variable v), $q(\mathbf{w}; v)$ and approximates the posterior $p(\mathbf{w}|\mathbf{D})$ by minimizing the KL divergence between $q(\mathbf{w}; v)$ and $p(\mathbf{w}|\mathbf{D})$, thus turning the posterior estimation into an optimization problem.

Our approach directly attempts to approximate $p(y|x, \mathbf{w})$ of a trained point prediction neural network. For doing so, we start with an RKHS embedding of the model weights, $\psi_{\mathbf{w}}$, which best approximates the weight PDF, for evaluating a particular model prediction y . We then use perturbation theory to express the local behavior of $\psi_{\mathbf{w}}$ around y as in terms of successive approximate uncertainty moments: $\psi_{\mathbf{w}}(y) = \psi_{\mathbf{w}}^0(y) + \lambda \psi_{\mathbf{w}}^1(y) + \lambda^2 \psi_{\mathbf{w}}^2(y) + \dots$, which characterize the degree of regularization of the model weights around y .

3 PERTURBATION THEORY

Perturbation theory is well known in quantum mechanical applications where it involves approximation methods to describe a complicated system as a perturbed version of a similar but simpler system whose mathematical solution is well known (Landau & Lifshitz, 2013). In doing so, the various physical quantities associated with the complicated system (energy levels and eigenstates) get expressed as *corrections* to the known quantities of the unperturbed system. We formally define the time-independent perturbation theory (Landau & Lifshitz, 1974) as follows:

Definition 1 (Rayleigh-Schrödinger perturbation theory)

Let us suppose that we desire to find approximate solutions of following time-independent system with Hamilto-

nian H for which it is difficult to find exact solutions (wavefunction ψ and energy E):

$$H\psi = E\psi \quad (2)$$

Let us assume that we know the exact solutions (ψ^0 and E^0) of a simpler system with Hamiltonian H_0 which arise from the time-independent Schrödinger equation as follows:

$$H_0\psi^0 = E^0\psi^0 \quad (3)$$

Here the subscript 0 denotes the quantities to be associated with an unperturbed system. Let H_p be a Hamiltonian representing a weak physical disturbance and let λ be a dimensionless parameter ranging between 0 (no perturbation) and 1 (full perturbation) so that the difference between H and H_0 is merely seen as perturbation on H_0 by λH_p . This leads to an expression of H as a perturbed Hamiltonian given by $H = H_0 + \lambda H_p$. We therefore require to find approximate solutions to the following Schrödinger's equation of the perturbed Hamiltonian by finding approximate expressions for wavefunction ψ and energy E :

$$H = (H_0 + \lambda H_p)\psi = E\psi \quad (4)$$

Assuming λ to be sufficiently weak, one can express E and ψ in terms of a power series starting from the unperturbed quantities leading to the following approximate solutions:

$$\begin{aligned} E &= E^0 + \lambda E^1 + \lambda^2 E^2 + \dots \\ \psi &= \psi^0 + \lambda \psi^1 + \lambda^2 \psi^2 + \dots \end{aligned} \quad (5)$$

where E^k and ψ^k are k^{th} order corrections to energy and wavefunction respectively.

4 PERTURBATION IN WEIGHT POTENTIAL FIELD

Our goal is to find the closest possible approximation to the true predictive PDF of the model at y given by $p(y|x, w)$. Let us assume that this ideal solution, represented by ψ_w , is a solution to an inherent system of weights represented by a Hamiltonian H_w . Our goal is therefore to find the solution to the following Schrödinger's equation:

$$H_w\psi_w = E_w\psi_w \quad (6)$$

Following the intuition of perturbation theory, we begin with a simpler system of weights described by a base-system Hamiltonian H_0 having a known solution that we choose as the kernel mean embedding (KME) of weights,

$\psi_w^0 = \mu_w = \int k(w, \cdot) d\mathbb{P}(\mathbf{w})$, because of its elegant properties as a non-parametric and universal quantifier of PDF (Berlinet & Thomas-Agnan, 2011; Muandet et al., 2017). We use the unbiased estimate of the KME (assuming no prior information on $\mathbb{P}(\mathbf{w})$) given by $\psi_w^0 = \hat{\mu}_w = \frac{1}{n} \sum_{t=1}^n k(w_t, \cdot)$, where n is the number of weights. Thus we use KME as an efficient functional estimator of the PDF of the trained weights (in the RKHS) and we are interested in quantifying the influence of the weight PDF in the prediction space of the model. We therefore evaluate the KME at a prediction y (assuming Gaussian kernel) which becomes the following:

$$\psi_w^0(y) = \frac{1}{n} \sum_{t=1}^n G_\sigma(w_t, y) \quad (7)$$

This is also termed as the *cross information potential field* (Principe et al., 2000; Singh & Principe, 2021) which evaluates the PDF at a data domain (prediction space in this case) that is different from the domain describing the PDF (model weights). Its name originates from the physical interpretation of ψ_w^0 if we think of the projected weights $G_\sigma(w_t, \cdot)$ as particles in a potential field that exerts an influence over an external object y . The Schrödinger's equation corresponding to the base-system Hamiltonian H_0 with the known solution ψ_w^0 becomes the following:

$$H_0\psi_w^0 = E_w^0\psi_w^0 \quad (8)$$

(8) therefore denotes a system that is controlled implicitly by the weights but which evaluates the dynamics at the model prediction space and is hence similar to the system defined by (6) whose solutions we desire. We want to add a perturbation to H_0 that shifts its evaluation from y to $y + \Delta y$. In doing so, we determine how regularized the system of weights is around y . A big change in system dynamics due to the perturbation would mean the weights are not regularized around y are hence the model uncertainty at y is high. Therefore we make the perturbation Hamiltonian H_p consist of a Laplacian operator (which is a local gradient based operator) that operates on y and denote it as ∇_y^2 . The intensity of the perturbation controls the size of neighborhood around y where the analysis is being made and hence is directly dependent on the kernel width we chose in the KME formulation ψ_w^0 for defining the weight PDF function in the unperturbed Hamiltonian H_0 . Therefore we construct perturbation Hamiltonian as $H_p = -\frac{\sigma^2}{2} \nabla_y^2$ so that $H = H_0 - \frac{\sigma^2}{2} \nabla_y^2$. This is similar to the part of the Hamiltonian referred to as the kinetic energy operator in the QIPF formulation in (Singh & Principe, 2021). Therefore the Schrödinger equation corresponding to the desired system Hamiltonian now becomes the

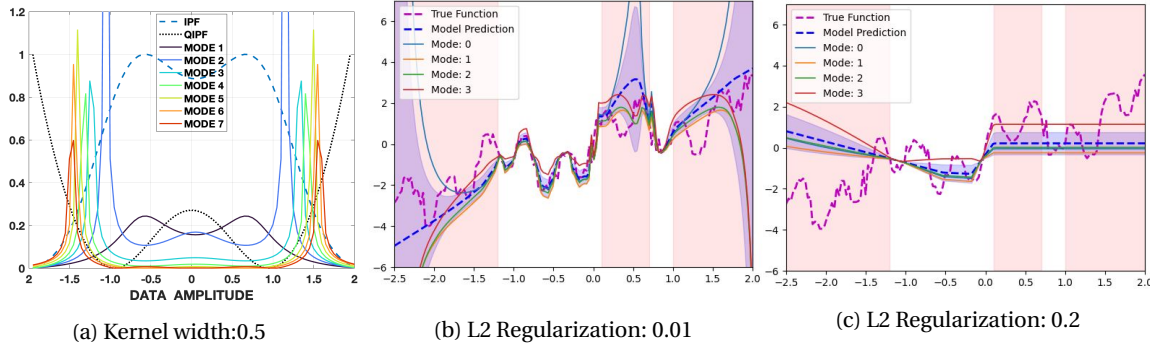


Figure 2: (a) QIPF modes of a sine-wave in data space. Tail regions of the PDF are seen to be efficiently quantified by QIPF modes. (b, c): Model uncertainty: (b) shows the high sensitivity of the QIPF with respect to model's seen and unseen data regions. (c) shows it to be well calibrated with model's regularization.

following:

$$H\psi_{\mathbf{w}} = \left(H_0 - \frac{\sigma^2}{2} \nabla_y^2\right) \psi_{\mathbf{w}} = E_{\mathbf{w}} \psi_{\mathbf{w}} \quad (9)$$

Here, its solution $\psi_{\mathbf{w}}$ is determined in terms of a power series expansion starting with the base-system (unperturbed) Hamiltonian solution $\psi_{\mathbf{w}}^0$ as follows:

$$\psi_{\mathbf{w}} = \psi_{\mathbf{w}}^0 + \lambda \psi_{\mathbf{w}}^1 + \lambda^2 \psi_{\mathbf{w}}^2 + \dots \quad (10)$$

where the perturbation intensities λ are simply the kernel width term $\frac{\sigma^2}{2}$ and $\psi_{\mathbf{w}}^1, \psi_{\mathbf{w}}^2, \dots$ are the successive orders of corrections to $\psi_{\mathbf{w}}^0$ in order to obtain $\psi_{\mathbf{w}}$.

Rearranging the terms of (9), we obtain the expression:

$$H_0 = E_{\mathbf{w}} + (\sigma^2/2) \frac{\nabla_y^2 \psi_{\mathbf{w}}}{\psi_{\mathbf{w}}} \quad (11)$$

which is exactly the same as the QIPF expressions in (Singh & Principe, 2021,0). Here, the Hamiltonian of the original undisturbed system, H_0 is the QIPF (V_s) in the expression given by eq. (3.2) in (Singh & Principe, 2020). Instead of doing a moment expansion of $E_{\mathbf{w}}$, for practical considerations and to determine H_0 uniquely, we simply let it be a lower bound given by $E_{\mathbf{w}} = -\min(\sigma^2/2) \frac{\nabla_y^2 \psi_{\mathbf{w}}}{\psi_{\mathbf{w}}}$ so that H_0 is always positive. It also makes sense from a viewpoint of continuous systems where discrete "energy levels" have no real meaning. We approximate the successive correction terms corresponding to the power series expansion of by projecting $\psi_{\mathbf{w}}^0$ to the successive orders of Hermite polynomials leading to the moment expansion expression

of H_0 as:

$$\begin{aligned} H_0^k &= E_{\mathbf{w}}^k + (\sigma^2/2) \frac{\nabla_y^2 \mathcal{P}_k(\psi_{\mathbf{w}}^0)}{\mathcal{P}_k(\psi_{\mathbf{w}}^0)} \\ &= E_{\mathbf{w}}^k + (\sigma^2/2) \frac{\nabla_y^2 \psi_{\mathbf{w}}^k}{\psi_{\mathbf{w}}^k} \end{aligned} \quad (12)$$

Here, $\mathcal{P}_k(\psi_{\mathbf{w}}) = \psi_{\mathbf{w}}^k$ is the projection of $\psi_{\mathbf{w}}$ in the k^{th} order normalized Hermite polynomial to obtain an approximation of $\psi_{\mathbf{w}}^k$ and $E_{\mathbf{w}}^k = -\min(\sigma^2/2) \frac{\nabla_y^2 \psi_{\mathbf{w}}^k}{\psi_{\mathbf{w}}^k}$. Through (12), the Hamiltonian of the desired system $H_{\mathbf{w}}$ is now expressed in terms of successive orders of corrections required for the base system Hamiltonian $H_{\mathbf{w}}^0$ to approximately become $H_{\mathbf{w}}$. Therefore, if there is large corrections required (corresponding to large values of higher order moments of H_0^k) at a particular prediction y , it will mean that the model is not confident enough about its implicit characterization of posterior PDF $p(y|x, w)$ at y . Therefore higher order moments of H_0^k (or the QIPF) represent successively quantify degrees of predictive uncertainty of the model.

Thus we have derived the QIPF expression of model uncertainty by following a quantum physical viewpoint of model weight-prediction relationship. The Hamiltonian $H_{\mathbf{w}}^k$ is therefore called the quantum information potential field (or the quantum cross-information potential field to be more specific) because it has been derived by applying quantum theoretical concepts (perturbation theory) on a field-based representation of the weight PDF in an RKHS.

5 ILLUSTRATIVE EXAMPLES

As a pedagogical example, we implement the QIPF decomposition of a simple sine-wave signal in Fig. 2a, where we show how the different moments of the QIPF behave in

the space of the signal PDF quantified in terms of empirical KME (IPF). It can be seen here that higher order modes successively quantify regions outside of the main signal PDF. This is a useful property for especially quantifying uncertainty outside of a data domain in situations involving covariate shift in the data.

In another example, we implement QIPF decomposition on an over-parameterized and fully connected multi-layer perceptron consisting of 3 hidden layers with 100 neurons in each layer that is trained on just 120 data pairs of a toy regression problem of learning a weighted sine-wave function with added noise. The training is carried out using different L2-regularization intensities (including no regularization that corresponds to a highly overfit model) using training samples that were generated only in the white regions. Pink regions represent regions with no training data. The model was tested in the entire data region $[-2, 2.5]$ and QIPF framework was implemented by extracting 4 modes and taking their average as the uncertainty range. At each test point, the mode values were added with the sample amplitude for easier visualization. As can be seen from Fig. 2b, uncertainty range quantified by the QIPF (blue shaded regions) is able to sensitively discriminate between seen (white) and unseen (pink) data regions by the model. As regularization is increased in Fig. 2c, the QIPF uncertainty ranges indicate that the model begins to become more confident outside of the training regions while sacrificing bias (indicated by increased QIPF uncertainty) inside the training zones. This indicates QIPF captures true posterior of model. We provide more examples in section A (appendix).

6 METHODS AND METRICS

For comparisons, we follow a similar experimental setup as done by [Ovadia et al. \(2019\)](#). We use established methods as comparison benchmarks that do not use prior information about the nature or intensity of test-set corruption to quantify model uncertainty under covariate shift and hence fall into the same category of methods as the QIPF. These methods are listed as follows.

- **MC Dropout:** Monte Carlo implementation of dropout during model testing ([Gal & Ghahramani, 2016](#); [Srivastava et al., 2014](#)).
- **MC Dropout LL:** MC dropout implemented only over the last model layer ([Riquelme et al., 2018](#)).
- **SVI:** Stochastic Variational Bayesian Inference ([Graves, 2011](#); [Blundell et al., 2015](#)).
- **SVI LL:** Stochastic Variational Bayesian Inference applied only to the last model layer ([Riquelme et al., 2018](#)).
- **Ensemble:** Ensembles of T (set as 10 here) networks independently trained with different random initial-

izations on the datasets ([Lakshminarayanan et al., 2017](#)).

We evaluate the UQ methods based on their ability to detect classification errors of the model in real time when fed with corrupted test data. We measure this ability in terms of areas under ROC and precision-recall (PR) curves associated with the error detection problem. We also evaluate calibration metrics of Brier score and expected calibration error, along with point biserial and Spearman correlation scores between quantified uncertainties and errors. These metrics are described in section B (appendix).

7 EXPERIMENTAL RESULTS

We used python 3.7 along with tensorflow library to perform all simulations. We utilized MNIST, K-MNIST (Kuzushiji-MNIST, a more challenging alternative to MNIST) ([Clanuwat et al., 2018](#)) and CIFAR-10 datasets for the comparative analysis of methods. For MNIST and K-MNIST, we used the regular 2-convolutional layer LeNet network architecture with standard training procedure and dataset split. We used two different networks for modeling CIFAR-10, one of them being a VGG-3 architecture consisting of 3 VGG convolution blocks (each consisting of two convolution layers followed by batch normalization, max pooling and dropout layers) and the other being ResNet-18. The successive blocks in VGG-3 consisted of 32, 64 and 128 filters respectively in each of their two layers. This was followed by two dense layers (with dropout in the middle) consisting of 128 and 10 nodes respectively. ReLu activation function was used here after each layer except the last, where Softmax was used. All networks were trained on uncorrupted datasets using Adam optimizer and categorical cross-entropy cost function. We achieved testing accuracies (on uncorrupted test-set) of 98.6% for MNIST, 91.9% for K-MNIST, 87.5% for CIFAR-10 (using VGG-3) and 91.5% for CIFAR-10 (using ResNet-18) thereby representing a diverse group of models.

To evaluate the UQ methods on the trained models, we corrupted the test-sets of datasets with different intensities using common corruption techniques ([Hendrycks & Dietterich, 2019](#)). Some of the corruption technique are illustrated in section C (appendix). For QIPF implementation, we first evaluated the cross - IPF given by (7) at each model's test prediction (the maximum last layer output value before softmax thresholding) in the field created by model weights. The number of weights used for cross-IPF computation were reduced by average pooling of weights at each layer so that we used only 1022 pooled weight values in LeNet, 2400 in VGG-3 and 3552 in ResNet. The kernel width was set as the bandwidth determined by the Silverman's rule ([Silverman, 2018](#)) multiplied by a factor that is determined through cross-validation over a part of the original/uncorrupted training dataset (found to be 80

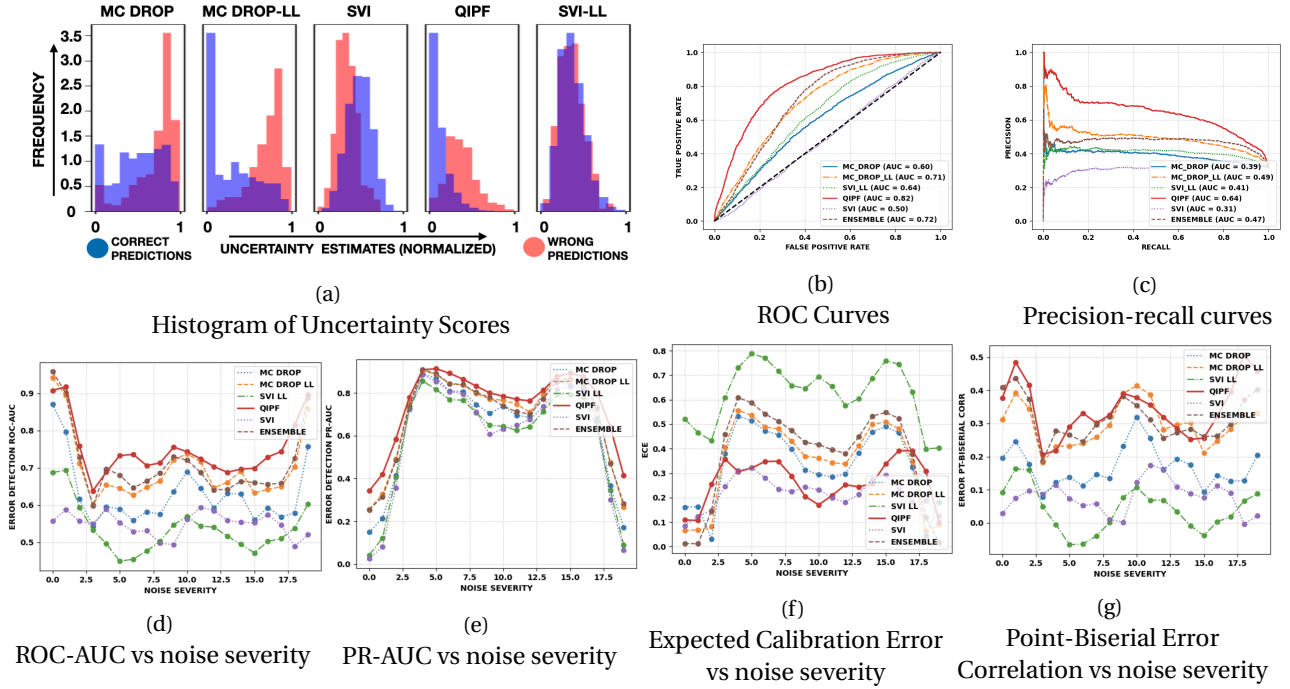


Figure 3: MNIST illustrative example: (a) shows the histograms of uncertainty estimates where QIPF can be seen to achieve better class-separation between correct and wrong predictions (very low overlap). (c) and (d) show corresponding error detection ROC and precision-recall curves, (e), (f) and (g) show the graphs of ROC-AUC, PR-AUC and PT-Biserial Corr. vs noise intensity. QIPF framework can be seen to have better performance.

in all cases). This was followed by computation of uncertainty modes of the QIPF (12). We extracted 4 QIPF modes for LeNet and VGG-3 models and 10 modes for ResNet-18. We took the average value of the modes at any prediction to be its uncertainty score. For other methods, we followed similar implementation strategy as [Ovadia et al. \(2019\)](#) and refer the reader to section D (appendix) for the details. We illustrate the QIPF implementation on MNIST in Fig. 11. Fig 11a shows the histogram plots of uncertainty estimates of the different methods corresponding to the correct test-set predictions (blue) and the wrong predictions (red), with the test-set being corrupted by 270 degrees of rotation. The class-separation ability of the QIPF decomposition framework can be seen to be significantly better than the other methods with the most frequent uncertainty score values for the correct and wrong predictions being further apart from each other when compared to other methods. This is also evident from the ROC and precision-recall (PR) curves associated with prediction error detection of the different uncertainty quantification methods in Fig. 11b and Fig. 11c respectively where the QIPF has the highest area under the curve (AUC) values. Fig. 11d and 11e show the ROC-AUC and PR-AUC associated with the UQ methods for different intensities/severity of rotation corruption. Also shown are the expected calibration errors and point-biserial correlation coefficients in Fig. 11f and 11g respectively between the test-set predic-

tion errors and the uncertainty estimates at each intensity. We observe here that the QIPF decomposition method performs significantly better over all other methods in terms of error detection as well as error correlation and calibration. Similar visualizations for other datasets/models are provided in section E (appendix). Table 1 summarizes the average ROC-AUC and PR-AUC values over all corruption intensities for different types of test-set corruptions for each dataset/model and UQ method. Best values are bolded in red and second best values in blue. Due to time limitations, we were unable to perform full SVI implementations on ResNet (those fields have thus been left blank). We can see here that the QIPF outperforms other methods in most cases (bolded in red) while ensemble method is seen to perform the second best, which is expected as it's been previously reported to be the state-of-the-art ([Ovadia et al., 2019](#)). Table 2 similarly summarizes the average expected calibrations errors and average brier scores of the different methods for different models. We see here that QIPF yields the best calibration values in most cases followed by stochastic variational inference. Similar tables for summarizing average correlation measures between the uncertainty estimates and the prediction errors are provided in section F (appendix).

CORRUPTION TYPE	DATASET	ROC-AUC						PR-AUC					
		MC-DROP	MC-DROP-LL	SVI	SVI-LL	ENSEMBLE	QIPF	MC-DROP	MC-DROP-LL	SVI	SVI-LL	ENSEMBLE	QIPF
ROTATION	MNIST	0.63 ± 0.08	0.70 ± 0.09	0.55 ± 0.03	0.66 ± 0.06	0.71 ± 0.09	0.75 ± 0.07	0.65 ± 0.23	0.69 ± 0.20	0.60 ± 0.27	0.67 ± 0.24	0.69 ± 0.20	0.75 ± 0.17
	K-MNIST	0.49 ± 0.02	0.52 ± 0.06	0.52 ± 0.01	0.54 ± 0.07	0.56 ± 0.11	0.58 ± 0.11	0.77 ± 0.22	0.79 ± 0.19	0.78 ± 0.21	0.80 ± 0.18	0.81 ± 0.14	0.84 ± 0.11
	CIFAR-10 (VGG-3)	0.58 ± 0.07	0.61 ± 0.08	0.53 ± 0.01	0.63 ± 0.05	0.57 ± 0.07	0.66 ± 0.04	0.68 ± 0.12	0.70 ± 0.11	0.65 ± 0.18	0.72 ± 0.15	0.66 ± 0.14	0.73 ± 0.17
	CIFAR-10 (RESNET-18)	0.49 ± 0.02	0.62 ± 0.07	-	0.60 ± 0.05	0.59 ± 0.06	0.64 ± 0.06	0.67 ± 0.14	0.75 ± 0.08	-	0.74 ± 0.10	0.72 ± 0.11	0.76 ± 0.10
BRIGHTNESS	MNIST	0.78 ± 0.09	0.87 ± 0.08	0.55 ± 0.04	0.78 ± 0.02	0.90 ± 0.06	0.87 ± 0.04	0.19 ± 0.12	0.29 ± 0.11	0.09 ± 0.13	0.18 ± 0.18	0.30 ± 0.16	0.35 ± 0.11
	K-MNIST	0.52 ± 0.04	0.56 ± 0.11	0.50 ± 0.02	0.55 ± 0.10	0.59 ± 0.16	0.60 ± 0.16	0.70 ± 0.34	0.73 ± 0.30	0.70 ± 0.34	0.72 ± 0.31	0.12 ± 0.11	0.14 ± 0.19
	CIFAR-10 (VGG-3)	0.69 ± 0.03	0.75 ± 0.11	0.52 ± 0.03	0.69 ± 0.07	0.69 ± 0.11	0.80 ± 0.11	0.44 ± 0.16	0.50 ± 0.16	0.32 ± 0.24	0.44 ± 0.19	0.41 ± 0.19	0.61 ± 0.12
	CIFAR-10 (RESNET-18)	0.47 ± 0.01	0.46 ± 0.00	-	0.57 ± 0.01	0.52 ± 0.01	0.50 ± 0.02	0.84 ± 0.01	0.84 ± 0.01	-	0.89 ± 0.01	0.89 ± 0.01	0.87 ± 0.01
SHEAR	MNIST	0.62 ± 0.10	0.68 ± 0.11	0.56 ± 0.03	0.63 ± 0.09	0.69 ± 0.11	0.70 ± 0.09	0.64 ± 0.23	0.68 ± 0.21	0.59 ± 0.27	0.64 ± 0.24	0.68 ± 0.22	0.71 ± 0.17
	K-MNIST	0.49 ± 0.03	0.55 ± 0.08	0.51 ± 0.02	0.59 ± 0.06	0.61 ± 0.12	0.64 ± 0.11	0.65 ± 0.25	0.69 ± 0.22	0.67 ± 0.26	0.71 ± 0.22	0.73 ± 0.17	0.77 ± 0.14
	CIFAR-10 (VGG-3)	0.63 ± 0.08	0.66 ± 0.09	0.57 ± 0.03	0.66 ± 0.04	0.62 ± 0.08	0.69 ± 0.02	0.66 ± 0.18	0.68 ± 0.16	0.62 ± 0.25	0.68 ± 0.20	0.64 ± 0.20	0.69 ± 0.24
	CIFAR-10 (RESNET-18)	0.52 ± 0.02	0.66 ± 0.08	-	0.64 ± 0.05	0.64 ± 0.06	0.68 ± 0.07	0.59 ± 0.17	0.71 ± 0.10	-	0.68 ± 0.14	0.67 ± 0.14	0.71 ± 0.10
ZOOM	MNIST	0.53 ± 0.12	0.58 ± 0.15	0.51 ± 0.02	0.58 ± 0.11	0.63 ± 0.14	0.70 ± 0.13	0.56 ± 0.27	0.60 ± 0.24	0.56 ± 0.30	0.60 ± 0.26	0.63 ± 0.24	0.72 ± 0.20
	K-MNIST	0.49 ± 0.04	0.54 ± 0.08	0.51 ± 0.02	0.58 ± 0.08	0.61 ± 0.13	0.65 ± 0.11	0.62 ± 0.26	0.65 ± 0.23	0.63 ± 0.26	0.68 ± 0.22	0.71 ± 0.17	0.75 ± 0.15
	CIFAR-10 (VGG-3)	0.59 ± 0.08	0.63 ± 0.09	0.56 ± 0.03	0.60 ± 0.08	0.58 ± 0.08	0.64 ± 0.08	0.67 ± 0.17	0.70 ± 0.15	0.65 ± 0.23	0.68 ± 0.17	0.65 ± 0.18	0.71 ± 0.17
	CIFAR-10 (RESNET-18)	0.52 ± 0.01	0.64 ± 0.07	-	0.63 ± 0.04	0.61 ± 0.06	0.65 ± 0.07	0.65 ± 0.17	0.73 ± 0.01	-	0.72 ± 0.14	0.70 ± 0.13	0.74 ± 0.12
SHIFT	MNIST	0.65 ± 0.13	0.73 ± 0.16	0.53 ± 0.03	0.67 ± 0.12	0.71 ± 0.18	0.77 ± 0.14	0.42 ± 0.28	0.49 ± 0.23	0.36 ± 0.32	0.43 ± 0.28	0.46 ± 0.24	0.59 ± 0.18
	K-MNIST	0.53 ± 0.05	0.66 ± 0.08	0.53 ± 0.01	0.69 ± 0.05	0.78 ± 0.10	0.81 ± 0.07	0.27 ± 0.17	0.36 ± 0.15	0.28 ± 0.18	0.38 ± 0.18	0.46 ± 0.11	0.57 ± 0.10
	CIFAR-10 (VGG-3)	0.75 ± 0.04	0.79 ± 0.03	0.53 ± 0.01	0.72 ± 0.02	0.72 ± 0.04	0.75 ± 0.02	0.37 ± 0.03	0.43 ± 0.04	0.24 ± 0.05	0.37 ± 0.05	0.34 ± 0.03	0.38 ± 0.10
	CIFAR-10 (RESNET-18)	0.56 ± 0.01	0.79 ± 0.01	-	0.71 ± 0.01	0.74 ± 0.01	0.78 ± 0.01	0.31 ± 0.28	0.54 ± 0.01	-	0.45 ± 0.01	0.44 ± 0.01	0.50 ± 0.01

Table 1: Average ROC-AUC values (left) and average PR-AUC values (right) of different methods for all datasets and corruption types over all corruption intensities. Best values are boldened in red and second best in blue.

CORRUPTION TYPE	DATASET	EXPECTED CALIBRATION ERROR						BRIER SCORE					
		MC-DROP	MC-DROP-LL	SVI	SVI-LL	ENSEMBLE	QIPF	MC-DROP	MC-DROP-LL	SVI	SVI-LL	ENSEMBLE	QIPF
ROTATION	MNIST	0.33 ± 0.15	0.39 ± 0.13	0.22 ± 0.06	0.65 ± 0.10	0.38 ± 0.30	0.26 ± 0.09	0.34 ± 0.11	0.32 ± 0.12	0.34 ± 0.05	0.81 ± 0.16	0.37 ± 0.14	0.35 ± 0.10
	K-MNIST	0.58 ± 0.18	0.47 ± 0.16	0.15 ± 0.03	0.79 ± 0.12	0.45 ± 0.16	0.09 ± 0.02	0.40 ± 0.09	0.39 ± 0.08	0.30 ± 0.02	0.98 ± 0.17	0.37 ± 0.09	0.22 ± 0.02
	CIFAR-10 (VGG-3)	0.33 ± 0.12	0.33 ± 0.11	0.14 ± 0.02	1.69 ± 0.43	0.42 ± 0.16	0.25 ± 0.07	0.29 ± 0.20	0.23 ± 0.13	0.23 ± 0.12	2.90 ± 4.09	0.54 ± 0.22	0.18 ± 0.15
	CIFAR-10 (RESNET-18)	0.36 ± 0.1	0.58 ± 0.15	-	0.58 ± 0.02	0.33 ± 0.11	0.18 ± 0.15	0.32 ± 0.05	0.48 ± 0.10	-	0.51 ± 0.11	0.25 ± 0.05	0.18 ± 0.10
SHEAR	MNIST	0.32 ± 0.14	0.33 ± 0.18	0.17 ± 0.04	0.59 ± 0.09	0.36 ± 0.20	0.24 ± 0.08	0.29 ± 0.11	0.29 ± 0.13	0.28 ± 0.04	0.72 ± 0.13	0.32 ± 0.15	0.30 ± 0.09
	K-MNIST	0.40 ± 0.15	0.38 ± 0.17	0.17 ± 0.03	0.72 ± 0.10	0.38 ± 0.18	0.10 ± 0.02	0.36 ± 0.10	0.35 ± 0.2	0.31 ± 0.02	0.88 ± 0.15	0.33 ± 0.11	0.21 ± 0.03
	CIFAR-10 (VGG-3)	0.33 ± 0.18	0.36 ± 0.18	0.16 ± 0.02	4.24 ± 0.98	0.36 ± 0.19	0.32 ± 0.18	0.42 ± 0.19	0.30 ± 0.15	0.07 ± 0.06	2.56 ± 1.28	0.09 ± 0.03	0.08 ± 0.24
	CIFAR-10 (RESNET-18)	0.25 ± 0.12	0.49 ± 0.18	-	0.62 ± 0.19	0.26 ± 0.15	0.24 ± 0.19	0.41 ± 0.07	0.55 ± 0.16	-	0.68 ± 0.10	0.37 ± 0.07	0.36 ± 0.12
ZOOM	MNIST	0.37 ± 0.18	0.35 ± 0.22	0.19 ± 0.06	0.70 ± 0.16	0.36 ± 0.25	0.73 ± 0.44	0.31 ± 0.14	0.30 ± 0.16	0.29 ± 0.05	0.84 ± 0.21	0.32 ± 0.18	0.97 ± 0.63
	K-MNIST	0.39 ± 0.17	0.37 ± 0.18	0.13 ± 0.07	0.67 ± 0.11	0.35 ± 0.19	0.12 ± 0.02	0.35 ± 0.11	0.33 ± 0.11	0.25 ± 0.05	0.81 ± 0.15	0.30 ± 0.12	0.18 ± 0.04
	CIFAR-10 (VGG-3)	0.34 ± 0.21	0.40 ± 0.18	0.16 ± 0.02	1.44 ± 0.80	0.41 ± 0.22	0.25 ± 0.17	0.52 ± 0.10	0.53 ± 0.12	0.26 ± 0.07	1.27 ± 0.84	0.46 ± 0.18	0.27 ± 0.07
	CIFAR-10 (RESNET-18)	0.28 ± 0.13	0.54 ± 0.18	-	1.08 ± 0.11	0.30 ± 0.17	0.18 ± 0.18	0.35 ± 0.05	0.52 ± 0.17	-	1.05 ± 0.81	0.34 ± 0.08	0.25 ± 0.14
SHIFT	MNIST	0.23 ± 0.15	0.20 ± 0.19	0.15 ± 0.07	0.59 ± 0.10	0.19 ± 0.22	0.20 ± 0.10	0.22 ± 0.12	0.19 ± 0.14	0.27 ± 0.06	0.69 ± 0.16	0.22 ± 0.18	0.29 ± 0.14
	K-MNIST	0.18 ± 0.05	0.13 ± 0.07	0.17 ± 0.01	0.55 ± 0.07	0.09 ± 0.09	0.08 ± 0.02	0.21 ± 0.07	0.18 ± 0.08	0.28 ± 0.01	0.64 ± 0.10	0.15 ± 0.09	0.18 ± 0.04
	CIFAR-10 (VGG-3)	0.07 ± 0.03	0.09 ± 0.02	0.17 ± 0.01	2.38 ± 0.60	0.05 ± 0.03	0.04 ± 0.03	0.35 ± 0.18	0.37 ± 0.14	0.39 ± 0.05	1.96 ± 0.92	0.16 ± 0.03	0.22 ± 0.05
	CIFAR-10 (RESNET-18)	0.1 ± 0.01	0.21 ± 0.02	-	1.07 ± 0.08	0.03 ± 0.01	0.53 ± 0.02	0.31 ± 0.28	0.34 ± 0.01	-	2.41 ± 0.65	0.11 ± 0.02	0.44 ± 0.02

Table 2: Average ECE (left) and average Brier scores (right) of different methods for all datasets and corruption types over all corruption intensities. Best values are boldened in red and second best in blue. Lower values are better.

8 COMPUTATIONAL COST DISCUSSION

MODEL	TIME (ms) PER TEST SAMPLE		
	MC DROP	MC DROP LL	QIPF
LeNeT	3.84	3.55	0.64
VGG-3	30.03	25.75	0.88
ResNet-18	51.33	39.72	1.86

Table 3: Computational time analysis

The only computational parts of QIPF are the cross-IPF ($\psi_{\mathbf{w}}$) which grows linearly with the number of weights and moment extraction growing linearly with the number of moments. The time complexity of the QIPF for each test iteration therefore becomes $\mathcal{O}(n + m)$, where n and m are the number of weights and number of moments respectively. However, we see here that we are able to outperform all methods with very low values of n (since we do average pooling of weights at the layers) and low value of m

(4 to 10 QIPF modes). This is unlike ensemble or Monte Carlo based methods such as MC dropout where reducing the number of sampling steps or size of ensembles has considerably negative effects on accuracy of uncertainty estimation. The compute times of our implementations of QIPF and MC dropout per test sample is shown in Table 3. It can be seen that QIPF is much faster.

9 CONCLUSION

In this paper, we showed that by viewing the weight PDF of a trained neural network as an RKHS based potential field, we can locally measure the interactions between the weights and the model predictions to yield precise estimates of predictive uncertainty in a computationally efficient manner. This is made possible by a principled use of the perturbation theory, which eventually yields the QIPF framework. We applied this approach on a important problem of uncertainty quantification in the presence of covariate shifts in the test data and showed that it outperforms established Bayesian and ensemble approaches across various metrics that measure the quality of uncertainty estimates. Furthermore, it is also significantly faster to compute and scales better existing approaches. In the future, we plan to extend the analysis of the framework to more large scale applications.

10 ACKNOWLEDGMENTS

This work was partially supported by DARPA under grant no. FA9453-18-1-0039 and ONR under grant no. N00014-21-1-2345.

References

- Amodei, D., Olah, C., Steinhardt, J., Christiano, P., Schulman, J., and Mané, D. Concrete problems in ai safety. *arXiv preprint arXiv:1606.06565*, 2016.
- Berlinet, A. and Thomas-Agnan, C. *Reproducing kernel Hilbert spaces in probability and statistics*. Springer Science & Business Media, 2011.
- Bishop, C. M. Bayesian methods for neural networks. 1995.
- Blundell, C., Cornebise, J., Kavukcuoglu, K., and Wierstra, D. Weight uncertainty in neural networks. *arXiv preprint arXiv:1505.05424*, 2015.
- Brier, G. W. et al. Verification of forecasts expressed in terms of probability. *Monthly weather review*, 78(1):1–3, 1950.
- Clanuwat, T., Bober-Irizar, M., Kitamoto, A., Lamb, A., Yamamoto, K., and Ha, D. Deep learning for classical japanese literature. *arXiv preprint arXiv:1812.01718*, 2018.
- DeGroot, M. H. and Fienberg, S. E. The comparison and evaluation of forecasters. *Journal of the Royal Statistical Society: Series D (The Statistician)*, 32(1-2):12–22, 1983.
- Gal, Y. and Ghahramani, Z. Dropout as a bayesian approximation: Representing model uncertainty in deep learning. In *international conference on machine learning*, pp. 1050–1059, 2016.
- Garipov, T., Izmailov, P., Podoprikin, D., Vetrov, D., and Wilson, A. G. Loss surfaces, mode connectivity, and fast ensembling of dnns. In *Proceedings of the 32nd International Conference on Neural Information Processing Systems*, pp. 8803–8812, 2018.
- Gast, J. and Roth, S. Lightweight probabilistic deep networks. In *Proceedings of the IEEE Conference on Computer Vision and Pattern Recognition*, pp. 3369–3378, 2018.
- Graves, A. Practical variational inference for neural networks. In *Advances in neural information processing systems*, pp. 2348–2356, 2011.
- Guo, C., Pleiss, G., Sun, Y., and Weinberger, K. Q. On calibration of modern neural networks. In *International Conference on Machine Learning*, pp. 1321–1330. PMLR, 2017.
- Hein, M., Andriushchenko, M., and Bitterwolf, J. Why relu networks yield high-confidence predictions far away from the training data and how to mitigate the problem. In *Proceedings of the IEEE/CVF Conference on Computer Vision and Pattern Recognition*, pp. 41–50, 2019.
- Hendrycks, D. and Dietterich, T. Benchmarking neural network robustness to common corruptions and perturbations. *arXiv preprint arXiv:1903.12261*, 2019.
- Hoffman, M. D., Blei, D. M., Wang, C., and Paisley, J. Stochastic variational inference. *The Journal of Machine Learning Research*, 14(1):1303–1347, 2013.
- Izmailov, P., Podoprikin, D., Garipov, T., Vetrov, D., and Wilson, A. G. Averaging weights leads to wider optima and better generalization. *arXiv preprint arXiv:1803.05407*, 2018.
- Kendall, A. and Gal, Y. What uncertainties do we need in bayesian deep learning for computer vision? *arXiv preprint arXiv:1703.04977*, 2017.
- Khan, M., Nielsen, D., Tangkaratt, V., Lin, W., Gal, Y., and Srivastava, A. Fast and scalable bayesian deep learning by weight-perturbation in adam. In *International Conference on Machine Learning*, pp. 2611–2620. PMLR, 2018.

- Kristiadi, A., Hein, M., and Hennig, P. Being bayesian, even just a bit, fixes overconfidence in ReLU networks. In III, H. D. and Singh, A. (eds.), *Proceedings of the 37th International Conference on Machine Learning*, volume 119 of *Proceedings of Machine Learning Research*, pp. 5436–5446. PMLR, 13–18 Jul 2020. URL <https://proceedings.mlr.press/v119/kristiadi20a.html>.
- Kuleshov, V., Fenner, N., and Ermon, S. Accurate uncertainties for deep learning using calibrated regression. In *International Conference on Machine Learning*, pp. 2796–2804. PMLR, 2018.
- Lakshminarayanan, B., Pritzel, A., and Blundell, C. Simple and scalable predictive uncertainty estimation using deep ensembles. In *Advances in Neural Information Processing Systems*, pp. 6402–6413, 2017.
- Landau, L. and Lifshitz, E. Chapter 4 - perturbation theory. In Landau, L. and Lifshitz, E. (eds.), *Quantum Mechanics*, pp. 116–135. Pergamon, 1974. ISBN 978-0-08-017801-1. <https://doi.org/10.1016/B978-0-08-017801-1.50010-5>. URL <https://www.sciencedirect.com/science/article/pii/B9780080178011500105>.
- Landau, L. D. and Lifshitz, E. M. *Quantum mechanics: non-relativistic theory*, volume 3. Elsevier, 2013.
- LeCun, Y., Bengio, Y., and Hinton, G. Deep learning. *nature*, 521(7553):436, 2015.
- Leonard, J., Kramer, M., and Ungar, L. A neural network architecture that computes its own reliability. *Computers & Chemical Engineering*, 16(9):819–835, 1992. ISSN 0098-1354. [https://doi.org/10.1016/0098-1354\(92\)80035-8](https://doi.org/10.1016/0098-1354(92)80035-8). An International Journal of Computer Applications in Chemical Engineering.
- Lu, Z., Ie, E., and Sha, F. Uncertainty estimation with infinitesimal jackknife, its distribution and mean-field approximation. *arXiv preprint arXiv:2006.07584*, 2020.
- Lundberg, S. and Lee, S.-I. A unified approach to interpreting model predictions. *arXiv preprint arXiv:1705.07874*, 2017.
- MacKay, D. J. A practical bayesian framework for back-propagation networks. *Neural computation*, 4(3):448–472, 1992.
- Maddox, W. J., Izmailov, P., Garipov, T., Vetrov, D. P., and Wilson, A. G. A simple baseline for bayesian uncertainty in deep learning. *Advances in Neural Information Processing Systems*, 32:13153–13164, 2019.
- Malinin, A. and Gales, M. Predictive uncertainty estimation via prior networks. *arXiv preprint arXiv:1802.10501*, 2018.
- Muandet, K., Fukumizu, K., Sriperumbudur, B., Schölkopf, B., et al. Kernel mean embedding of distributions: A review and beyond. *Foundations and Trends® in Machine Learning*, 10(1-2):1–141, 2017.
- Naeini, M. P., Cooper, G., and Hauskrecht, M. Obtaining well calibrated probabilities using bayesian binning. In *Twenty-Ninth AAAI Conference on Artificial Intelligence*, 2015.
- Neal, R. M. *Bayesian learning for neural networks*, volume 118. Springer Science & Business Media, 2012.
- Osband, I., Blundell, C., Pritzel, A., and Van Roy, B. Deep exploration via bootstrapped dqn. In *Advances in neural information processing systems*, pp. 4026–4034, 2016.
- Ovadia, Y., Fertig, E., Ren, J., Nado, Z., Sculley, D., Nowozin, S., Dillon, J. V., Lakshminarayanan, B., and Snoek, J. Can you trust your model’s uncertainty? evaluating predictive uncertainty under dataset shift. *arXiv preprint arXiv:1906.02530*, 2019.
- Paisley, J., Blei, D., and Jordan, M. Variational bayesian inference with stochastic search. *arXiv preprint arXiv:1206.6430*, 2012.
- Pearce, T., Zaki, M., Brintrup, A., and Neel, A. Uncertainty in neural networks: Bayesian ensembling. *arXiv preprint arXiv:1810.05546*, 2018.
- Pradier, M. F., Pan, W., Yao, J., Ghosh, S., and Doshi-Velez, F. Latent projection bnns: Avoiding weight-space pathologies by learning latent representations of neural network weights. *arXiv preprint arXiv:1811.07006*, 2018.
- Principe, J. C., Xu, D., Fisher, J., and Haykin, S. Information theoretic learning. *Unsupervised adaptive filtering*, 1: 265–319, 2000.
- Quionero-Candela, J., Sugiyama, M., Schwaighofer, A., and Lawrence, N. D. *Dataset shift in machine learning*. The MIT Press, 2009.
- Riquelme, C., Tucker, G., and Snoek, J. Deep bayesian bandits showdown: An empirical comparison of bayesian deep networks for thompson sampling. *arXiv preprint arXiv:1802.09127*, 2018.
- Silverman, B. W. *Density estimation for statistics and data analysis*. Routledge, 2018.
- Singh, R. and Principe, J. C. Time series analysis using a kernel based multi-modal uncertainty decomposition framework. In *Conference on Uncertainty in Artificial Intelligence*, pp. 1368–1377. PMLR, 2020.
- Singh, R. and Principe, J. C. Toward a kernel-based uncertainty decomposition framework for data and models. *Neural Computation*, 33(5):1164–1198, 2021. ISSN

0899-7667. 10.1162/neco_a_01372. URL https://doi.org/10.1162/neco_a_01372.

Smola, A. J. and Schölkopf, B. *Learning with kernels*, volume 4. Citeseer, 1998.

Srivastava, N., Hinton, G., Krizhevsky, A., Sutskever, I., and Salakhutdinov, R. Dropout: a simple way to prevent neural networks from overfitting. *The journal of machine learning research*, 15(1):1929–1958, 2014.

Tibshirani, R. A comparison of some error estimates for neural network models. *Neural Computation*, 8(1):152–163, 1996.

A ILLUSTRATIVE EXAMPLES

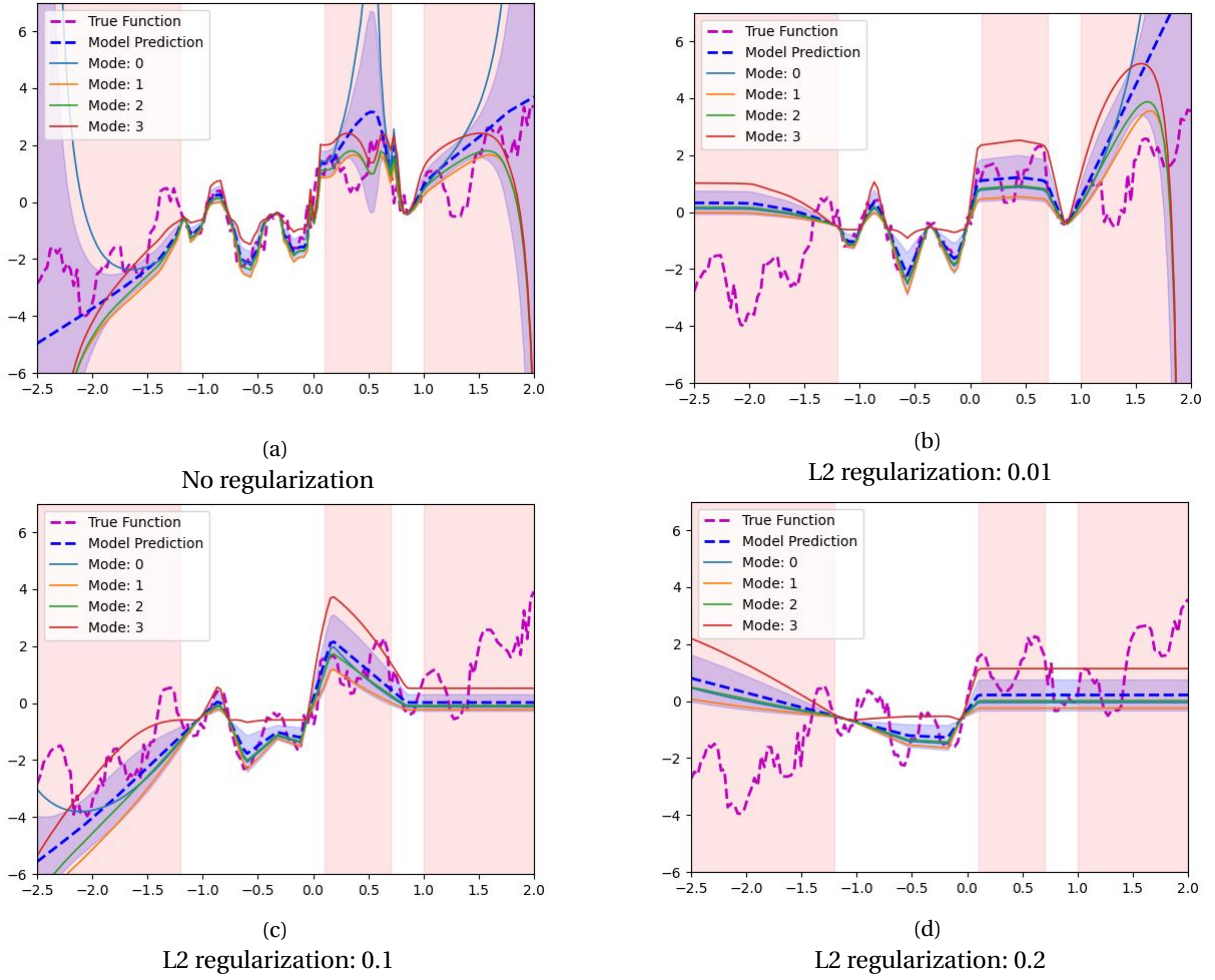


Figure 4: More Regularization examples

B METRICS FOR COMPARING UNCERTAINTY MEASURES

Apart from metrics such as ROC - AUC and PR - AUC for evaluating the capability of detecting prediction errors, we also compute two calibration metrics for the different UQ methods which are the expected calibration error (ECE) and Brier score. Here we measure the calibration of the highest probability value in the prediction layer with respect to model's prediction error. The metrics described as follows:

B.1 EXPECTED CALIBRATION ERROR

Expected calibration error measures the difference between a neural network's prediction probability estimate and its accuracy (Naeini et al., 2015). Suppose all the confidence scores of the test-set are binned into K distinct bins, then it is the average gap between within bucket accuracy and within bucket predicted confidence (pseudo-probability) given as:

$$ECE = \sum_{k=1}^K \frac{|B_k|}{N} |acc(B_k) - conf(B_k)|$$

where, $acc(B_k) = |B_k|^{-1} \sum_{k \in B_k} [y_k = \hat{y}_k]$ and $conf(B_k) = |B_k|^{-1} \sum_{k \in B_k} p(\hat{y}_k | x_k, \mathbf{w})$ and $\hat{y}_k = \argmax_y p(y | x_k, \mathbf{w})$.

B.2 BRIER SCORE

Brier score (Brier et al., 1950) is strictly proper scoring function (unlike ECE) that measures the accuracy of the predicted probabilities. It is the squared error of the predicted probability $p(\hat{y}|x, \mathbf{w})$ and one-hot encoded true response, y given by:

$$BS = |Y|^{-1} \sum_{y \in Y} (p(\hat{y}|x, \mathbf{w}) - \delta(\hat{y} - y))^2$$

It also has a decomposed interpretation as $BS = \text{uncertainty} - \text{resolution} + \text{reliability}$ (DeGroot & Fienberg, 1983).

B.3 EXAMPLE DATA CORRUPTIONS

Some corruption types at different intensities are shown in Fig. 5 for samples of MNIST dataset.

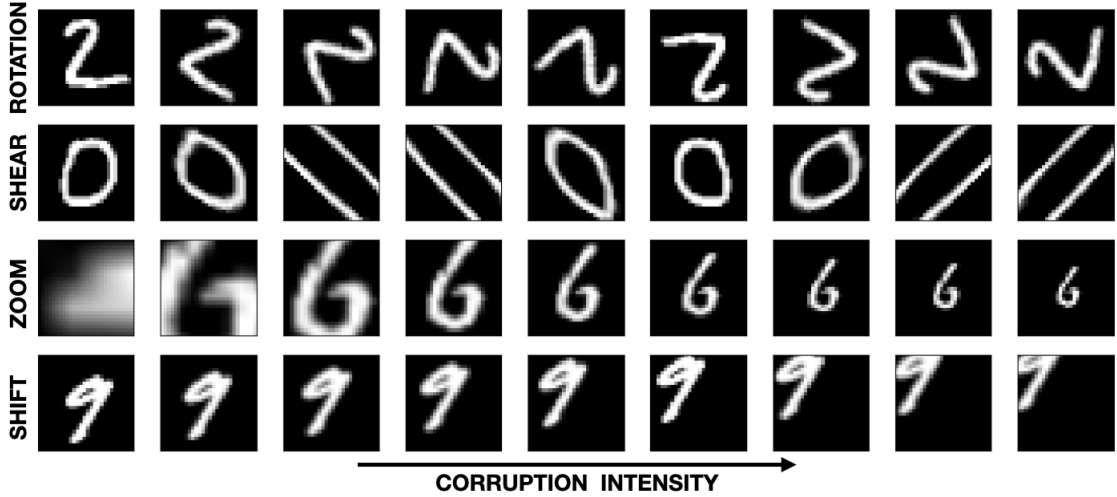


Figure 5: Data corruption types at different intensities.

C IMPLEMENTATION STRATEGY OF METHODS

C.1 STOCHASTIC VARIATIONAL INFERENCE

For implementing the Stochastic Variational Inference algorithm (Blundell et al., 2015), we replaced each dense layer and the last convolutional layer in the network with Flipout layers. We used independent (mean-field) Gaussian distributions for prior initializations of standard deviations and implemented negative log-likelihood Bayesian optimization to obtain the posteriors using 100 epochs.

For implementing SVI-LL (last layer) algorithm, we replaced only the last dense layer with a Flipout layer and implemented the same optimization procedure as before with 50 epochs.

C.2 MONTE-CARLO DROPOUT

For implementation of MC-Dropout, we introduced a dropout layer (during testing) after each convolutional block (before the next convolutional layer) and before each dense layer. We implemented 100 stochastic forward runs. The standard deviation of the results of all runs at each prediction was considered to be the uncertainty score. We varied the dropout rates between 0.01 and 0.4 and found that the best results were obtained by using a rate of 0.1 for LeNet models and 0.2 for VGG-3 model, which we used as benchmarks.

The same implementation strategy was followed for MC-Dropout-LL (last layer), except that only a single dropout layer was introduced in the network before the last dense layer during testing. It was observed that the dropout rate of 0.2 corresponded to the best result for all models, which we used as benchmarks.

C.3 ENSEMBLE

For implementing the Ensemble methods, we trained 10 models with random initializations for each dataset and computed the standard deviation of results as the uncertainty score.

D ADDITIONAL RESULT FIGURES

D.1 KMNIST

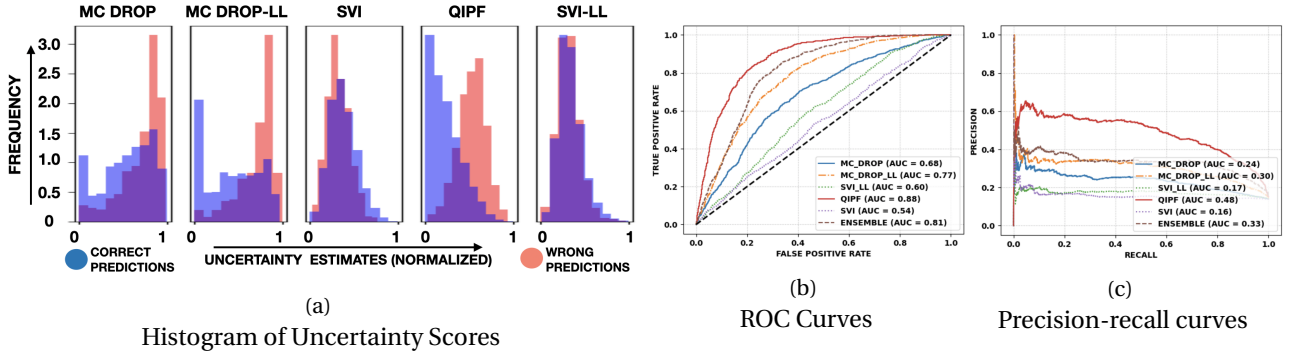


Figure 6: KMNIST Brightness Corrupted: Intensity = 40%

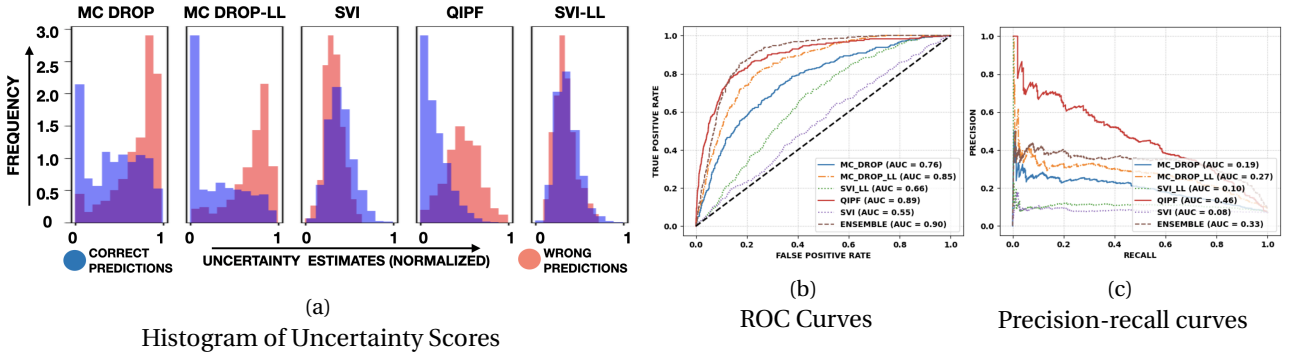


Figure 7: KMNIST Rotation Corrupted: Intensity = 10%

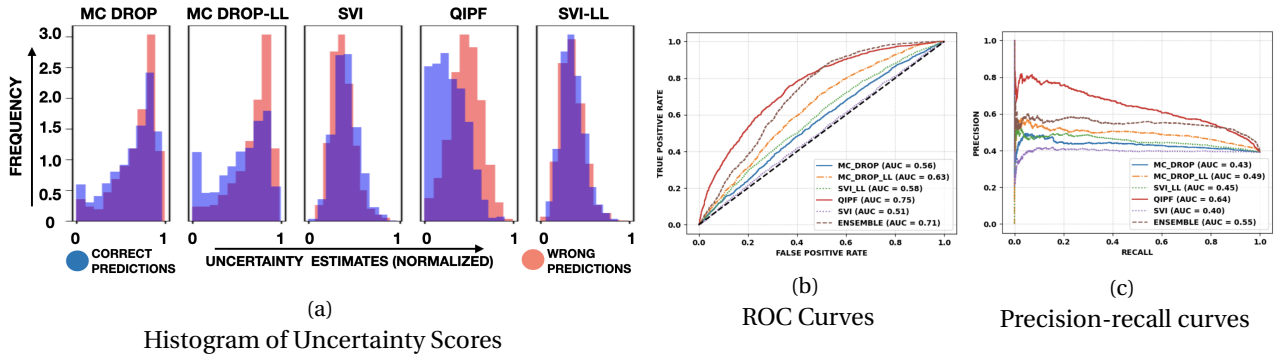


Figure 8: KMNIST Shear Corrupted: Intensity = 90%

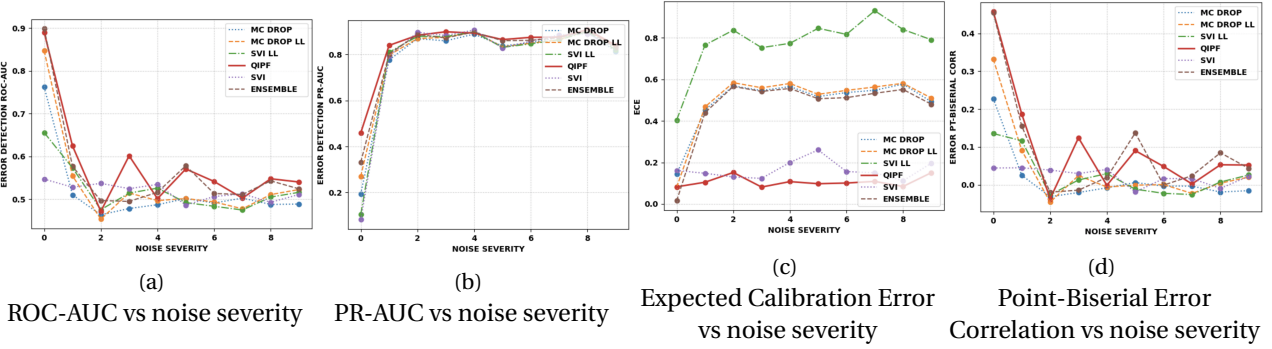


Figure 9: KMNIST: Rotation Corruption (All intensities)

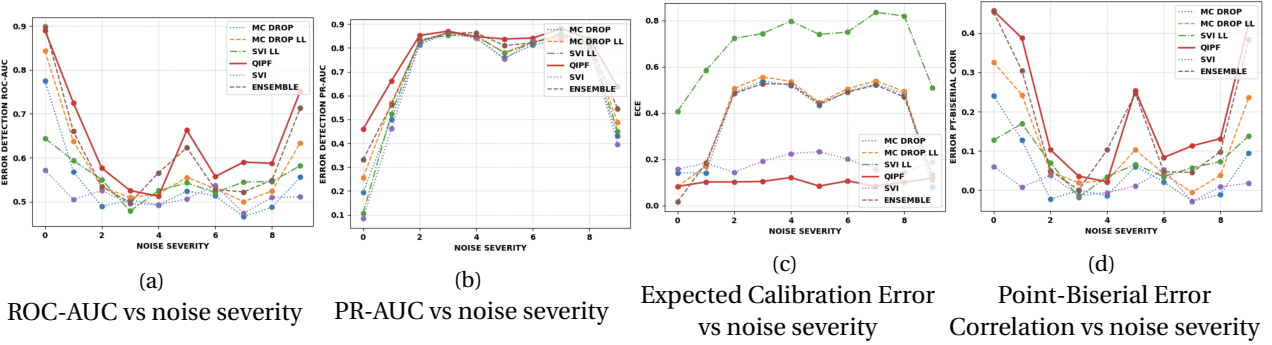


Figure 10: KMNIST: Shear Corruption (All intensities)

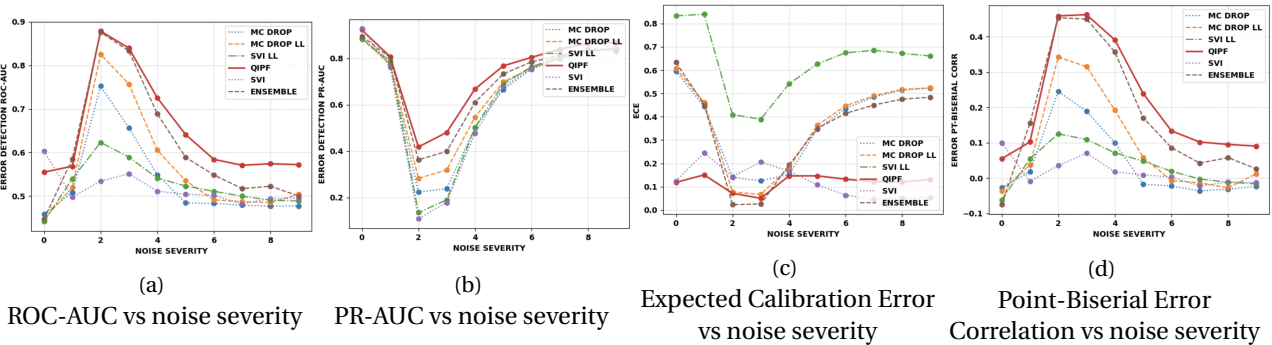
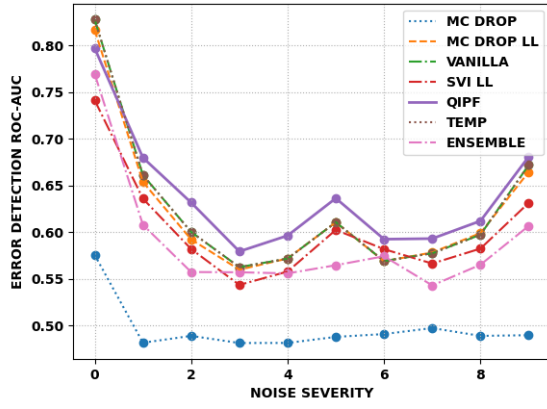
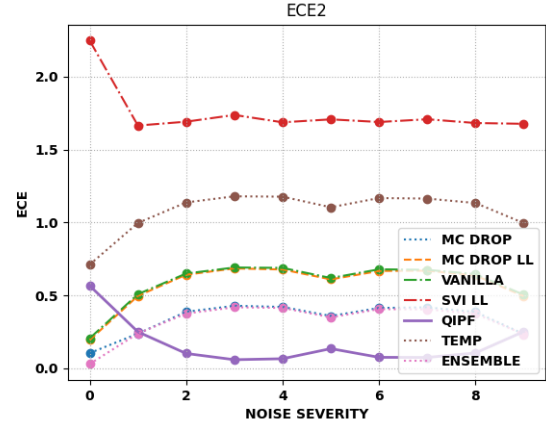


Figure 11: KMNIST: Zoom Corruption (All intensities)

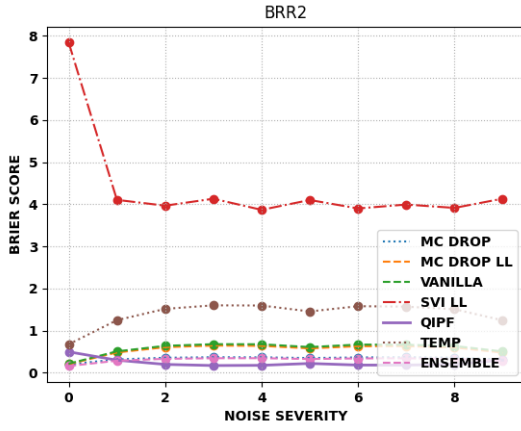
D.2 CIFAR-10 (RESNET-18)



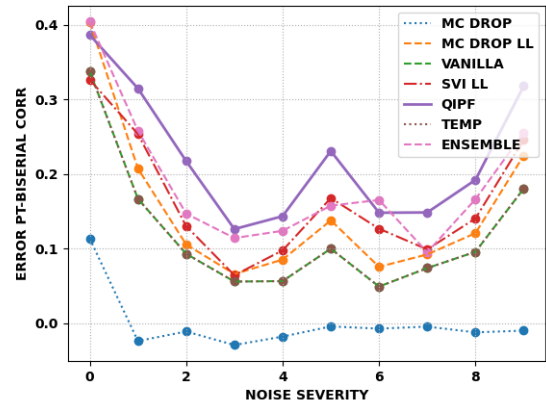
(a) ROC-AUC vs Noise Severity



(b) Expected Calibration Error vs Noise Severity



(c) Brier Score vs Noise Severity



(d) Point Biserial Correlation with error vs Noise Severity

Figure 12: CIFAR 10: ResNet-18 - rotation corruption (all intensities)

E ERROR CORRELATION RESULTS

We evaluate how correlated the uncertainty estimates of the different methods are with respect to the model prediction error by using point-biserial correlation coefficient which measures correlation between a continuous variable (uncertainty quantified by the different techniques) and a dichotomous variable (model prediction error). We also evaluate Spearman coefficient. results are shown in Table 4.

CORRUPTION TYPE	DATASET	POINT BISERIAL CORRELATION						SPEARMAN CORRELATION					
		MC-DROP	MC-DROP-LL	SVI	SVI-LL	ENSEMBLE	QIPF	MC-DROP	MC-DROP-LL	SVI	SVI-LL	ENSEMBLE	QIPF
ROTATION	MNIST	0.16 ± 0.06	0.29 ± 0.06	0.08 ± 0.05	0.24 ± 0.05	0.31 ± 0.06	0.34 ± 0.08	0.16 ± 0.06	0.26 ± 0.07	0.06 ± 0.05	0.22 ± 0.05	0.27 ± 0.06	0.33 ± 0.07
	K-MNIST	0.00 ± 0.02	0.03 ± 0.08	0.03 ± 0.02	0.06 ± 0.10	0.09 ± 0.15	0.11 ± 0.08	0.01 ± 0.02	0.03 ± 0.08	0.03 ± 0.02	0.06 ± 0.10	0.08 ± 0.13	0.10 ± 0.15
	CIFAR-10 (VGG-3)	0.13 ± 0.09	0.19 ± 0.11	0.06 ± 0.02	0.21 ± 0.05	0.12 ± 0.08	0.24 ± 0.11	0.11 ± 0.02	0.17 ± 0.10	0.06 ± 0.02	0.20 ± 0.06	0.10 ± 0.08	0.25 ± 0.08
	CIFAR-10 (RESNET-18)	0.00 ± 0.03	0.15 ± 0.09	-	0.16 ± 0.08	0.18 ± 0.08	0.22 ± 0.08	0.00 ± 0.04	0.18 ± 0.11	-	0.16 ± 0.08	0.14 ± 0.09	0.22 ± 0.10
SHEAR	MNIST	0.16 ± 0.10	0.26 ± 0.14	0.08 ± 0.05	0.17 ± 0.10	0.26 ± 0.11	0.28 ± 0.11	0.15 ± 0.10	0.23 ± 0.12	0.07 ± 0.04	0.17 ± 0.10	0.24 ± 0.11	0.27 ± 0.10
	K-MNIST	0.00 ± 0.03	0.06 ± 0.08	0.01 ± 0.02	0.13 ± 0.08	0.17 ± 0.16	0.20 ± 0.15	0.00 ± 0.10	0.06 ± 0.08	0.01 ± 0.02	0.12 ± 0.08	0.14 ± 0.14	0.18 ± 0.13
	CIFAR-10 (VGG-3)	0.20 ± 0.10	0.25 ± 0.11	0.10 ± 0.04	0.24 ± 0.06	0.20 ± 0.08	0.25 ± 0.12	0.18 ± 0.10	0.23 ± 0.11	0.09 ± 0.03	0.24 ± 0.06	0.17 ± 0.09	0.28 ± 0.06
	CIFAR-10 (RESNET-18)	0.03 ± 0.03	0.21 ± 0.11	-	0.23 ± 0.06	0.26 ± 0.09	0.28 ± 0.09	0.04 ± 0.04	0.26 ± 0.13	-	0.22 ± 0.08	0.21 ± 0.10	0.28 ± 0.10
ZOOM	MNIST	0.01 ± 0.10	0.08 ± 0.14	0.01 ± 0.02	0.08 ± 0.10	0.17 ± 0.15	0.27 ± 0.17	0.01 ± 0.11	0.06 ± 0.13	0.01 ± 0.02	0.08 ± 0.10	0.15 ± 0.12	0.24 ± 0.15
	K-MNIST	0.00 ± 0.04	0.05 ± 0.09	0.01 ± 0.02	0.11 ± 0.10	0.18 ± 0.17	0.22 ± 0.15	0.00 ± 0.04	0.05 ± 0.09	0.01 ± 0.02	0.11 ± 0.10	0.15 ± 0.16	0.21 ± 0.14
	CIFAR-10 (VGG-3)	0.14 ± 0.13	0.20 ± 0.14	0.08 ± 0.04	0.14 ± 0.10	0.12 ± 0.11	0.19 ± 0.10	0.13 ± 0.12	0.19 ± 0.14	0.08 ± 0.04	0.15 ± 0.11	0.11 ± 0.11	0.22 ± 0.13
	CIFAR-10 (RESNET-18)	0.02 ± 0.02	0.17 ± 0.10	-	0.21 ± 0.06	0.20 ± 0.10	0.22 ± 0.10	0.03 ± 0.02	0.22 ± 0.13	-	0.20 ± 0.07	0.17 ± 0.10	0.23 ± 0.11
SHIFT	MNIST	0.11 ± 0.07	0.24 ± 0.11	0.02 ± 0.02	0.16 ± 0.09	0.23 ± 0.16	0.33 ± 0.15	0.12 ± 0.07	0.21 ± 0.10	0.02 ± 0.02	0.16 ± 0.10	0.18 ± 0.12	0.27 ± 0.12
	K-MNIST	0.03 ± 0.04	0.19 ± 0.06	0.04 ± 0.01	0.24 ± 0.04	0.39 ± 0.07	0.44 ± 0.05	0.02 ± 0.05	0.19 ± 0.06	0.03 ± 0.01	0.24 ± 0.04	0.35 ± 0.07	0.40 ± 0.05
	CIFAR-10 (VGG-3)	0.35 ± 0.02	0.42 ± 0.05	0.05 ± 0.01	0.28 ± 0.01	0.31 ± 0.02	0.27 ± 0.12	0.35 ± 0.02	0.41 ± 0.01	0.05 ± 0.02	0.31 ± 0.01	0.31 ± 0.02	0.36 ± 0.13
	CIFAR-10 (RESNET-18)	0.09 ± 0.01	0.39 ± 0.01	-	0.31 ± 0.01	0.37 ± 0.01	0.38 ± 0.00	0.09 ± 0.01	0.46 ± 0.01	-	0.33 ± 0.01	0.37 ± 0.02	0.43 ± 0.01

Table 4: Average Point Biserial correlation (left) and average Spearman correlation (right) coefficients (with respect to prediction errors) of different methods for all datasets and corruption types over all corruption intensities. Best values are boldened in red and second best in blue.